Evaluating the Conservation of Energy Variables in Simulations of Deep Moist Convection

JOHN M. PETERS[a] AND DANIEL R. CHAVAS[b]

[a] *Department of Meteorology, Naval Postgraduate School, Monterey, California*
[b] *Department of Earth, Atmospheric, and Planetary Sciences, Purdue University, West Lafayette, Indiana*

(Manuscript received 19 November 2020, in final form 17 May 2021)

ABSTRACT: It is often assumed in parcel theory calculations, numerical models, and cumulus parameterizations that moist static energy (MSE) is adiabatically conserved. However, the adiabatic conservation of MSE is only approximate because of the assumption of hydrostatic balance. Two alternative variables are evaluated here: MSE − IB and MSE + KE, wherein IB is the path integral of buoyancy (B) and KE is kinetic energy. Both of these variables relax the hydrostatic assumption and are more precisely conserved than MSE. This article quantifies the errors that result from assuming that the aforementioned variables are conserved in large-eddy simulations (LES) of both disorganized and organized deep convection. Results show that both MSE − IB and MSE + KE better predict quantities along trajectories than MSE alone. MSE − IB is better conserved in isolated deep convection, whereas MSE − IB and MSE + KE perform comparably in squall-line simulations. These results are explained by differences between the pressure perturbation behavior of squall lines and isolated convection. Errors in updraft B diagnoses are universally minimized when MSE − IB is assumed to be adiabatically conserved, but only when moisture dependencies of heat capacity and temperature dependency of latent heating are accounted for. When less accurate latent heat and heat capacity formulae were used, MSE − IB yielded poorer B predictions than MSE due to compensating errors. Our results suggest that various applications would benefit from using either MSE − IB or MSE + KE instead of MSE with properly formulated heat capacities and latent heats.

KEYWORDS: Convective clouds; Cumulus clouds; Thermodynamics

1. Introduction

Adiabatically conserved variables simplify a variety of calculations and derivations, and are therefore ubiquitous in research and forecasting. Common examples of such variables include the following:

- Moist static energy (MSE): the sum of enthalpy and gravitational potential energy (e.g., Kiefer 1941; Riehl and Malkus 1958; Kreitzberg 1964).
- Liquid static energy (LSE) or liquid ice static energy (LISE) (e.g., Emanuel 1994; Khairoutdinov and Randall 2003). Note that LSE and LISE are simply rearrangements of MSE.
- Entropic variables: moist entropy s_m (Emanuel 1994; Pauluis and Held 2002), equivalent potential temperature θ_e (e.g., Romps and Kuang 2010), liquid (and ice) water potential temperature θ_l (e.g., Bryan and Fritsch 2004), pseudoadiabatic entropy s_p, pseudoadiabatic θ_p (e.g., Bolton 1980; Emanuel 1994), etc.

A common application of conserved variables is the computation of convective available potential energy (CAPE) in forecasting and parameterization, wherein it is frequently assumed that θ_e, θ_p, or MSE is conserved in a lifted air parcel. In cumulus parameterizations (CPs) and in entraining CAPE calculations (ECAPE; Zhang and McFarlane 1991; Zhang 2009; Peters et al. 2020b), it is often assumed that the only source/sink term for MSE or s_m is mixing (e.g., see discussion [e.g., see discussion surrounding Eq. (53) in Arakawa and Schubert (1974)]. For constant mixing rates, this assumption simplifies the computation of the vertical profiles of temperature (T), buoyancy (B), and other cloud properties that are important to CPs. Dynamical cores of cloud resolving models frequently use LISE as a prognostic thermodynamic variable, and assume Lagrangian sources/sinks of LISE only come from subgrid-scale mixing and radiation [e.g., the System for Atmospheric Modeling (SAM; Khairoutdinov and Randall 2003)]. This assumption consolidates prognostic thermodynamic variables and therefore makes model integration more efficient.

Entropic variables have been extensively analyzed in past literature, and a variety of formulas for s_m and θ_e exist ranging from approximate to exact. The situations where entropic variables are not adiabatically conserved are also well documented (e.g., Pauluis and Held 2002; Bryan and Fritsch 2004), and thus we have a proficient understanding of the limitations of these variables. In contrast, though it is known that the adiabatic conservation of MSE, LSE, and LISE is only approximate, few attempts have been made to quantify the errors resulting from assuming these variables are adiabatically conserved. Furthermore, there are various approximations for the precise definition of these variables, but the consequences of the various approximations have not been extensively studied.

In fact, the following energy variables that are more precisely adiabatically conserved than MSE, but have received comparatively little attention in research and forecasting:

Corresponding author: J. Peters, jmpeters@nps.edu

DOI: 10.1175/JAS-D-20-0351.1

- MSE − IB: the sum of MSE and a parcel's vertically integrated buoyancy (IB)[1] (Romps 2015).
- Total energy: the sum of MSE and kinetic energy (KE) (hereafter MSE + KE; e.g., Darkow 1968; Sun and Sun 2019).

How do MSE − IB and MSE + KE improve upon assuming MSE alone is conserved? It was shown by Romps (2015) that MSE − IB is exactly conserved in parcel theory, wherein it is (necessarily) assumed that an air parcel's pressure is equal to that of the horizontally invariant background environment. This assumption implies that pressure perturbations p' vanish at the parcel location. Romps (2015) demonstrated by use of idealized adiabatic parcel calculations that calculations of lifted parcel T and B will incur high biases when one assumes MSE is conserved, and that these biases are corrected when one instead assumes MSE − IB is conserved. However, parcels traveling in a three-dimensional atmosphere could experience substantial p' leading to adiabatic errors even when one assumes that MSE − IB is conserved, along with open system sources and sinks of mass and energy. It is reasonable to hypothesize that adiabatic errors will still be larger when MSE is conserved in the presence of nonzero p' and open system effects, relative to when MSE − IB is assumed to be conserved, but this hypothesis requires validation in a large-eddy simulation (LES). A less likely, albeit possible, alternative outcome is that compensating errors related to the neglect of p' when MSE − IB is assumed to be conserved make it impractical to replace MSE with MSE − IB in research and forecasting applications.

In scenarios where flow is approximately steady, such as in mountain waves (e.g., Sun and Sun 2015) and tropical cyclones (TCs; e.g., Sun and Sun 2019, hereafter SS19), MSE + KE is advantageous because it accounts for exchanges between MSE and KE induced by p' that are neglected when MSE alone is conserved. However, one must assume steady-state flow in order to derive the exact adiabatic conservation of MSE + KE, and it is unclear how this assumption affects the accuracy of MSE + KE relative to MSE or MSE − IB in deep convection. For instance, deep convection often comprises series of rising ring vortex-like circulations, which are known as thermals (e.g., Sherwood et al. 2013; Romps and Charn 2015; Lebo and Morrison 2015; Hernandez-Deckers and Sherwood 2016; Morrison et al. 2020; Peters et al. 2020a), and thermals are decidedly unsteady. However, organized modes of deep convection such as supercells (e.g., Rotunno and Klemp 1982) and squall lines (e.g., Bryan and Parker 2010) often exhibit quasi-steady p' features. Hence, it is not obvious which variable may be better conserved given the presence of both steady and nonsteady p' in different modes of deep convection.

To address the aforementioned knowledge gaps, this paper provides a comprehensive comparison of the energy variables MSE, MSE + KE, and MSE − IB using both theory and analyses of LES. We address the following questions:

1) Is there an advantage to assuming MSE, MSE − IB, or MSE + KE is adiabatically conserved in deep convection?
2) What is responsible for the differences in how well each of these variables are conserved?
3) How does the adiabatic conservation of these variables depend on convective organization?
4) Do these conclusions differ when using simplified formulations for latent heats and heat capacities?

In addition to the simple academic exercise of comparing the three energy variables discussed in this section, our analysis provides insight for improving CPs and numerical models. For instance, it is possible (and often trivial) to modify most CPs and numerical model calculations that presently rely on MSE to account for the −IB or +KE terms.

The paper organization is as follows. We first detail the approximations used to derive the conservation laws for MSE, MSE − IB, and MSE + KE (section 2). We then assess errors related to these quantities along parcel trajectories in LESs of disorganized and organized deep convection cases (sections 3 and 4). Our conclusions are summarized in section 5.

2. Energy conservation laws

We may write the Lagrangian tendency for any arbitrary thermodynamic variable ψ as follows:

$$\frac{d\psi}{dt} = A_\psi + \varepsilon_\psi, \tag{1}$$

where A_ψ is the tendency from adiabatic processes, and ε_ψ represents all open system sources and sinks of ψ, such as mixing, precipitation exchanges, radiation, and surface fluxes. For ψ to be considered adiabatically conserved, there must exist conditions/assumptions under which $A_\psi \to 0$; thus an adiabatically conserved variable only has sources and sinks from open system effects.

To derive equations analogous to Eq. (1) for the conserved variables discussed in the introduction, we begin with the first law of thermodynamics for an ideal gas:

$$\frac{dk}{dt} = \frac{1}{\rho}\frac{dp}{dt} + \varepsilon_k, \tag{2}$$

where k is specific enthalpy, p is pressure, and ρ is density. The term $(1/\rho)dp/dt$ represents adiabatic sources and sinks of k from pressure-volume work [i.e., $A_k = (1/\rho)dp/dt$]. For moist air, k may be written as the sum of sensible heat and latent heat [e.g., Eq. (4.5.4) in Emanuel (1994)]:

$$k = [(1 - q_t)c_{pd} + q_t c_l]T + L_v q_v - L_i q_i, \tag{3}$$

where c_{pd} and c_l are the specific heat capacities at constant pressure of dry air and liquid water, respectively; q_v, q_l, q_i, and

[1] Romps (2015) referred to IB, which is the integral of buoyancy from the parcel height to any arbitrary fixed height, as convective available potential energy (CAPE). However, the standard definition of CAPE in most other past literature is the integral of the positive buoyancy of a lifted parcel between the level of free convection (LFC) and the equilibrium level (EL). To avoid confusion, we will refer to the buoyancy integrated over arbitrary vertical bounds as IB, and use CAPE to describe the integral of buoyancy between the LFC and EL.

$q_t = q_v + q_l + q_i$ are the mass fractions of water vapor, liquid water, ice water, and total water, respectively; $L_v = L_{v,\mathrm{ref}} + (T - T_{\mathrm{ref}})(c_{pv} - c_l)$ and $L_i = L_{i,\mathrm{ref}} + (T - T_{\mathrm{ref}})(c_l - c_i)$ are the temperature dependent latent heats of vaporization and freezing, respectively, obtained from Kirchoff's relations; and c_{pv} and c_i are the specific heat capacities of water vapor and ice, respectively.

Substituting Eq. (3) into Eq. (2) gives

$$\frac{d}{dt}(\mathrm{MSE} - gz) = \frac{1}{\rho}\frac{dp}{dt} + \varepsilon_k, \tag{4}$$

where g is gravity and MSE is defined following Romps [(2016), Eq. (6) therein] as follows:

$$\mathrm{MSE} \equiv k + gz = [(1 - q_t)c_{pd} + q_t c_l]T + L_v q_v - L_i q_i + gz. \tag{5}$$

To change Eq. (4) into a form that will be more convenient for later derivations, we write state variables as the sum of a hydrostatically balanced reference pressure $p_0(z)$ and density $\rho_0(z)$, and local deviations from this reference state $p'(x, y, z, t) \equiv p(x, y, z, t) - p_0(z)$ and $\rho'(x, y, z, t) \equiv \rho(x, y, z, t) - \rho_0(z)$. We also define $B \equiv -g(\rho'/\rho)$ and the vertical air velocity $w \equiv dz/dt$. Using these substitutions and definitions, we may rewrite Eq. (4) (without approximation) as follows:

$$\frac{d}{dt}(\mathrm{MSE}) = -wB + \frac{1}{\rho}\frac{dp'}{dt} + \varepsilon_k. \tag{6}$$

Hence, $A_{\mathrm{MSE}} = -wB + (1/\rho)(dp'/dt)$. These adiabatic source and sink terms together represent pressure-volume work due to perturbations ρ' and p', respectively, from the horizontally uniform hydrostatic reference state. These perturbations will result in pressure-volume work done by the parcel that is not directly exchangeable with gravitational potential energy, and will therefore serve as an adiabatic source or sink of MSE. Equation (6) is fully consistent with the governing equations of the numerical model that will be analyzed later, and thus will serve as a benchmark for assessing the error of subsequent approximate expressions. We may therefore use Eq. (6) to isolate open system parcel tendencies by simply solving for ε_k in Eq. (6):

$$\varepsilon_k = \frac{d}{dt}(\mathrm{MSE}) + wB - \frac{1}{\rho}\frac{dp'}{dt}. \tag{7}$$

In our numerical model configuration, ε_k encapsulates mixing from subgrid-scale turbulence, implicit diffusion from the advection scheme, and mass exchanges from hydrometeors. In later trajectory analysis, we evaluate Eq. (7) with quantities directly output along model trajectories. Note that the formula for B in the numerical model that will be used later is

$$B = g\left[\frac{\theta - \theta_0}{\theta_0} + \left(\frac{R_v}{R_d} - 1\right)(q_v - q_0) - (q_l + q_i)\right], \tag{8}$$

where θ is potential temperature, R_d is the dry gas constant, and R_v is the moist gas constant. This formula is used in all calculations in lieu of $B = -g(\rho'/\rho)$ for consistency with the numerical model.

a. Conservation of MSE

Recall that in the previous subsection, we define the reference state to be hydrostatically balanced, such that $dp_0/dz = -\rho_0 g$, but the parcel need not be. A common assumption is that the parcel itself is also hydrostatically balanced, such that $dp/dz = -\rho g$. This assumption conveniently results in $A_{\mathrm{MSE}} = -wB + (1/\rho)dp'/dt = 0$ and thus MSE is adiabatically conserved:

$$\frac{d}{dt}(\mathrm{MSE}) = \varepsilon_k. \tag{9}$$

The convenience of Eq. (9) for computing lifted parcel properties becomes apparent if we temporarily assume that $\varepsilon_k = w\epsilon(\mathrm{MSE}_0 - \mathrm{MSE})$, where ϵ is a constant fractional entrainment per length scale, and MSE_0 is the MSE of the background environment. We also write $d/dt = w(d/dz)$, where d/dz is the Lagrangian vertical derivative along the air parcel's path, to obtain the following:

$$\frac{d}{dz}(\mathrm{MSE}) = \epsilon(\mathrm{MSE}_0 - \mathrm{MSE}). \tag{10}$$

Equation (10) can be solved analytically for MSE, and this and similar equations are consequently ubiquitous among CPs (e.g., Arakawa and Schubert 1974; Zhang and McFarlane 1995) and in ECAPE calculations (e.g., Zhang and McFarlane 1991; Zhang 2009). Once a vertical profile of MSE has been obtained via Eq. (10), one may readily obtain profiles for T and q_v by making assumptions about parcel saturation, and by invoking the Clausius–Clapeyron relation.

b. Conservation of MSE − IB

In parcel theory, the "environment" surrounding an air parcel is often assumed to consist of the horizontally invariant reference state. In this situation, it is mathematically intractable to accurately characterize p', and hence the $(1/\rho)dp'/dt$ is neglected. Applying this assumption reduces Eq. (6) to

$$\frac{d}{dt}(\mathrm{MSE} - \mathrm{IB}) = \varepsilon_k, \tag{11}$$

where $\mathrm{IB}(z) \equiv \int_{z^*=z_i}^{z^*=z} B\,dz^* = \int_{t^*=t_i}^{t^*=t} wB\,dt^*$, where z_i and t_i are any arbitrary initial heights and times, respectively; and z and t are the current heights and times of the parcel, respectively. Alternatively (and without approximation), we may write the following:

$$\frac{d\mathrm{MSE}}{dz} = -B + \frac{\varepsilon_k}{w}, \tag{12}$$

where d/dz is the rate of change of a quantity as a parcel changes its height. This formula states that a rising air parcel loses MSE with height at a rate equal to B. Equation (12) loses some of the convenience of Eqs. (9) and (10) because it is no longer analytically solvable for MSE as a function of height. However, a Crank–Nicholson-like implicit integration scheme can be used to solve for the T of a lifted air parcel using Eq. (12) (as was discussed in Romps 2015), and Eq. (12) is therefore usable in CPs (e.g., Romps 2016). Equation (12) could be implemented as a prognostic thermodynamic equation in a

numerical model by simply adding a $-wB$ term to the right-hand side of the prognostic MSE equation. In fact, for applications of the anelastic approximation where atmospheric state variables at a given height are computed using the background pressure (i.e., p_0), MSE − IB becomes strictly conserved (Pauluis 2008).

c. Conservation of MSE + KE

To obtain the conservation equation for MSE + KE (e.g., SS19), we start with the three-dimensional momentum equation written as follows:

$$\frac{\partial \mathbf{V}}{\partial t} + (\mathbf{V}\cdot\nabla)\mathbf{V} = -\frac{1}{\rho}\nabla p - g\hat{k} + \boldsymbol{\varepsilon}_{\text{mom}}, \tag{13}$$

where $\mathbf{V}$ is the three-dimensional wind vector and the vector $\boldsymbol{\varepsilon}_{\text{mom}}$ represents mixing of momentum. We once again make use of a hydrostatically balanced background pressure p_0 and density ρ_0, and substitute $-(1/\rho)\nabla p - g\hat{k} = -(1/\rho)\nabla p' + B\hat{k}$. We also make use of the vector identity $-(\mathbf{V}\cdot\nabla)\mathbf{V} = -\nabla(\mathbf{V}\cdot\mathbf{V}/2) - (\nabla\times\mathbf{V})\times\mathbf{V}$ to write the following:

$$\frac{\partial \mathbf{V}}{\partial t} = -\nabla \text{KE} - (\nabla\times\mathbf{V})\times\mathbf{V} - \frac{1}{\rho}\nabla p' + B\hat{k} + \boldsymbol{\varepsilon}_{\text{mom}}, \tag{14}$$

where $\text{KE} \equiv \mathbf{V}\cdot\mathbf{V}/2$ is kinetic energy. By forming the inner product of $\mathbf{V}$ with Eq. (14) and noting that $\mathbf{V}\cdot(\nabla\times\mathbf{V})\times\mathbf{V} = 0$, we obtain the Lagrangian tendency equation for KE:

$$\frac{d\text{KE}}{dt} = -\frac{1}{\rho}\mathbf{V}\cdot\nabla p' + wB + \varepsilon_{\text{KE}}, \tag{15}$$

where $\varepsilon_{\text{KE}} \equiv \mathbf{V}\cdot\boldsymbol{\varepsilon}_{\text{mom}}$ represents mixing of KE. We note that $\mathbf{V}\cdot\nabla p' = dp'/dt - \partial p'/\partial t$, which allows Eq. (15) to be written as follows:

$$\frac{d\text{KE}}{dt} = -\frac{1}{\rho}\frac{dp'}{dt} + wB + \varepsilon_{\text{KE}} + \frac{1}{\rho}\frac{\partial p'}{\partial t}. \tag{16}$$

Combining Eq. (16) with Eq. (6) and rearranging gives

$$\frac{d}{dt}(\text{MSE} + \text{KE}) = \frac{1}{\rho}\frac{\partial p'}{\partial t} + \varepsilon_{\text{TE}}, \tag{17}$$

where $\varepsilon_{\text{TE}} = \varepsilon_k + \varepsilon_{\text{KE}}$. Hence, $A_{\text{MSE + KE}} = (1/\rho)\partial p'/\partial t$. If we assume that the local pressure is steady [i.e., $(1/\rho)\partial p'/\partial t \to 0$], we obtain the following:

$$\frac{d}{dt}(\text{MSE} + \text{KE}) = \varepsilon_{\text{TE}}. \tag{18}$$

We obtain ε_{KE} by solving Eq. (16) for this term in an analogous manner to how Eq. (6) was solved for ε_k in Eq. (7), and evaluating individual terms in Eq. (16) with quantities directly output along trajectories.

d. Why do MSE, MSE − IB, and MSE + KE differ?

All three formulae for conserved energy variables may be written as budget equations for MSE. For instance, when we assume MSE alone is conserved, we may divide Eq. (9) by w and vertically integrate from z_i to an arbitrary height z to obtain the following:

$$\text{MSE}_{\text{pred,MSE}}(z) = \text{MSE}_{\text{traj}}(z_i) + \int_{z^*=z_i}^{z^*=z} \frac{\varepsilon_{k,\text{traj}}}{w_{\text{traj}}} dz^*, \tag{19}$$

where the subscript "pred" indicate predictions of a quantity, the subscripts "traj" indicate direct output onto a trajectory from the simulations, and the subscript "MSE" indicates a prediction that assumes MSE is adiabatically conserved. Subtracting $\text{MSE}_{\text{traj}}(z)$ from both sides of the equation and combining with Eq. (7), where $d/dt = w(d/dz)$, gives

$$\text{err}_{\text{MSE}}(z) = \text{IB}_{\text{traj}}(z) - \int_{z^*=z_i}^{z^*=z} \frac{1}{\rho_{\text{traj}}}\frac{dp'}{dz}_{\text{traj}} dz^*, \tag{20}$$

where $\text{err}_{\text{MSE}}(z) \equiv \text{MSE}_{\text{pred,MSE}}(z) - \text{MSE}_{\text{traj}}(z)$ is the adiabatic error of our prediction as a function of height. Similarly, for MSE − IB and MSE + KE we obtain the following:

$$\text{err}_{\text{MSE−IB}}(z) = -\int_{z^*=z_i}^{z^*=z} \frac{1}{w_{\text{traj}}\rho_{\text{traj}}}\frac{dp'}{dt}_{\text{traj}} dz^*, \tag{21}$$

and

$$\text{err}_{\text{MSE+KE}}(z) = -\int_{z^*=z_i}^{z^*=z} \frac{1}{w_{\text{traj}}\rho_{\text{traj}}}\frac{\partial p'}{\partial t}_{\text{traj}} dz^*, \tag{22}$$

where $\text{err}_{\text{MSE−IB}}(z)$ and $\text{err}_{\text{MSE+KE}}(z)$ are errors from assuming MSE − IB and MSE + KE are conserved, respectively. These error formulae reveal that MSE − IB neglects the Lagrangian derivative of p', whereas MSE + KE neglects the local derivative of p'. MSE on the other hand neglects both IB and the Lagrangian derivative of p'. Since all p' terms are generally smaller in magnitude than IB as noted earlier, one expects that MSE − IB and MSE + KE should be more precisely conserved in deep convection than MSE. However, it remains unclear whether MSE − IB or MSE + KE should have an advantage over the other from these formulae.

To further explore the error behavior of MSE − IB versus MSE + KE, we examine the behavior of each in a simple toy model example of a rising parcel interacting with an idealized p' distribution. We demonstrate how the magnitude of errors related to each of these variables differs depending on how the p' distribution rises relative to the parcel. For an adiabatic parcel that rises purely vertically, Eq. (15) may be rewritten as follows:

$$\frac{d\text{KE}}{dz} = \frac{d}{dz}\left(\frac{w^2}{2}\right) = B - \frac{1}{\rho}\frac{\partial p'}{\partial z}. \tag{23}$$

From this equation we may also predict w and the height of the parcel as a function of time via numerical integration. Furthermore, our error terms in Eqs. (21) and (22) may be written for this scenario, assuming the initial $p' = 0$, as follows:

$$\text{err}_{\text{MSE−IB}}(z) = -\frac{p'_{\text{traj}}(z)}{\rho_{\text{traj}}}, \tag{24}$$

and

$$\text{err}_{\text{MSE+KE}}(z) = -\frac{p'_{\text{traj}}(z)}{\rho_{\text{traj}}} + \frac{1}{\rho_{\text{traj}}}\int_{z^*=z_i}^{z^*=z} \frac{\partial p'}{\partial z}_{\text{traj}} dz^*. \tag{25}$$

For simplicity, we have assumed a constant $\rho = 1\,\mathrm{kg\,m^{-3}}$. Note that while $\mathrm{err}_{\mathrm{MSE+KE}}$ would appear to have more error terms than $\mathrm{err}_{\mathrm{MSE-IB}}$, the second error term can partially offset the first; if p' is perfectly steady, the two p' terms cancel each other and the error term is zero. Hence, the nature of the errors for each depend on the steadiness of the pressure distribution along the parcel path, which we demonstrate using our toy model experiment.

We assume that this parcel experiences a constant positive $B = 0.1\,\mathrm{m\,s^{-2}}$, and as it rises it interacts with a p' dipole that is negative below and positive above (e.g., Figs. 1a–c). The p' is specified as $p' = \hat{p}\sin[\pi(z - z_{\mathrm{cent}})/H]$ for $|(z - z_{\mathrm{cent}})/H| < 1$, and $p' = 0\,\mathrm{Pa}$ elsewhere, with $\hat{p} = 10\,\mathrm{Pa}$, $H = 1500\,\mathrm{m}$, and z_{cent} initially at 1500 m. These parameter values are arbitrary, but reasonable variations in these values do not affect our qualitative interpretation of the forthcoming analysis. The center height of the p' dipole z_{cent} is assumed to ascend at a rate proportional to the w of the parcel, such that $dz_{\mathrm{cent}}/dt = \lambda w$ and $0 \le \lambda \le 1$. Hence, λ is a direct measure of the steadiness of p': $\lambda = 0$ represents a steady p' distribution ($\partial p'/\partial t = 0$) and $\lambda = 1$ represents an unsteady p' distribution that rises perfectly in concert with the parcel ($dp'/dt = 0$); intermediate values represent a mix of the two regimes.

Let us first consider the unsteady case of $\lambda = 1$, where the p' dipole rises at the same rate as the parcel with the parcel fixed at the center (Fig. 1a). In this case, $p' = 0$ for the parcel's entire path of ascent because the parcel is consistently positioned between the positive and negative p'. However, if we assume that MSE + KE is conserved, then we incorrectly infer from Eq. (23) that the parcel loses MSE at a rate of $-B + (1/\rho)\partial p'/\partial z$, which results in error accumulation with height (Fig. 1d). In this case, we are mistakenly assuming that the parcel does pressure-volume work related to the local vertical gradient in p', when in reality $p' = 0$ for the parcel. The steady state assumption underlying MSE + KE is what leads to these errors, since this assumption does not account for the nonsteady rise of the p' features. If, however, we assume that MSE − IB is conserved, we correctly infer that the parcel loses MSE at a rate of $-B$ because Lagrangian changes in p' are correctly assumed to be zero, and thus no error accumulation with height occurs (Fig. 1d).

Next, consider the steady case of $\lambda = 0$, where the p' dipole is fixed in time and the parcel rises through it (Fig. 1c). As the parcel rises through the dipole, its p' transitions from negative to positive. Within the bottom half of the region of anomalously low pressure, it will be accelerated upward by the upward pressure gradient acceleration while simultaneously doing pressure-volume work as p' decreases, hence losing MSE and gaining KE. This process reverses as the parcel rises between the centers of each p' region in the dipole. In this situation, we correctly infer that MSE decreases at a rate of $-B + (1/\rho)\partial p'/\partial z$ with height when MSE + KE is conserved. However, when MSE − IB is assumed to be conserved, we incorrectly infer that MSE decreases at a rate of $-B$, because we have neglected pressure–volume work from p' (Fig. 1g).

Finally, consider an intermediate case with intermediary values of λ (e.g., Fig. 1b), where both the parcel and the pressure dipole rise, but the parcel rises faster (e.g., Fig. 10 in Morrison and Peters 2018). Convection is also unsteady in this case, but p' felt by the parcel does not vanish. Neither MSE − IB or MSE + KE are precisely conserved and both produce comparable errors in this situation (Figs. 1e,f).

An examination of the errors over a range of λ values indeed shows that errors are larger for MSE + KE for $\lambda > 0.5$ and larger for MSE − IB for $\lambda < 0.5$ (Fig. 1h). Thus, whether MSE − IB or MSE + KE is more advantageous as an adiabatically conserved variable depends on whether the p' distribution is more or less steady. However, these errors are not symmetric: conservation errors for MSE + KE for $\lambda > 0.5$ are much larger than errors in MSE − IB for $\lambda < 0.5$. This asymmetry arises because the errors in MSE + KE accumulate continuously throughout the entire parcel ascent (Fig. 1d) because of the integral in Eq. (25), whereas the errors in MSE − IB are localized to the layer containing the p' dipole (Fig. 1g), as is apparent in Eq. (24). This asymmetry hints at a general advantage of MSE − IB over MSE + KE, which we elaborate upon later in our analysis of LESs.

As will be shown in later simulations, it is common for both steady and non-steady p' features to occur simultaneously in deep convection. To account for this behavior, we amended the toy model in a simple way to make it better emulate the numerical simulations by superposing with a steady background pressure that is constant for all λ. This steady background pressure was specified as $p' = \hat{p}\sin[2\pi(2000 - z)/1000]$, set to 0 Pa below 2 km and above 10 km, which was added to the already discussed pressure distributions. It featured a steady p' distribution with negative p' at low altitudes, and positive p' at higher altitudes, with the same magnitudes as the rising p' dipole. The addition of this background steady p' distribution only marginally increased the errors associated with MSE − IB (Figs. 1d–h), and did not change the general pattern of errors for both MSE − IB and MSE + KE. For instance, most errors related to MSE + KE ranged from marginally smaller than MSE − IB near $\lambda = 0.55$, to substantially larger than MSE − IB above $\lambda = 0.65$.

e. Common approximations for MSE

The formula for MSE is often simplified to facilitate computations and derivations. For instance, most applications that we are aware of neglect the influence of moisture on parcel heat capacity and assume constant latent heats (e.g., Riehl and Malkus 1958; Khairoutdinov and Randall 2003; Agard and Emanuel 2017), giving

$$\mathrm{MSE}_{\mathrm{cc}} \equiv c_{pd}T + L_{v,0}q_v - L_{i,0}q_i + gz\,, \tag{26}$$

where the subscript "cc" stands for "constant coefficients." This assumption will neglect the exchanges among specific heat capacity of air and latent heats as the parcel rises and cools. Ice is commonly neglected in Eq. (26), giving

$$\mathrm{MSE}_{\mathrm{cc,ni}} \equiv c_{pd}T + L_{v,0}q_v + gz\,, \tag{27}$$

where the "ni" part of the subscript stands for "no ice."

How might these approximations influence parcel properties such as T and B as a parcel undergoes vertical displacements? The heat capacity for moist air is larger than that of dry air by a

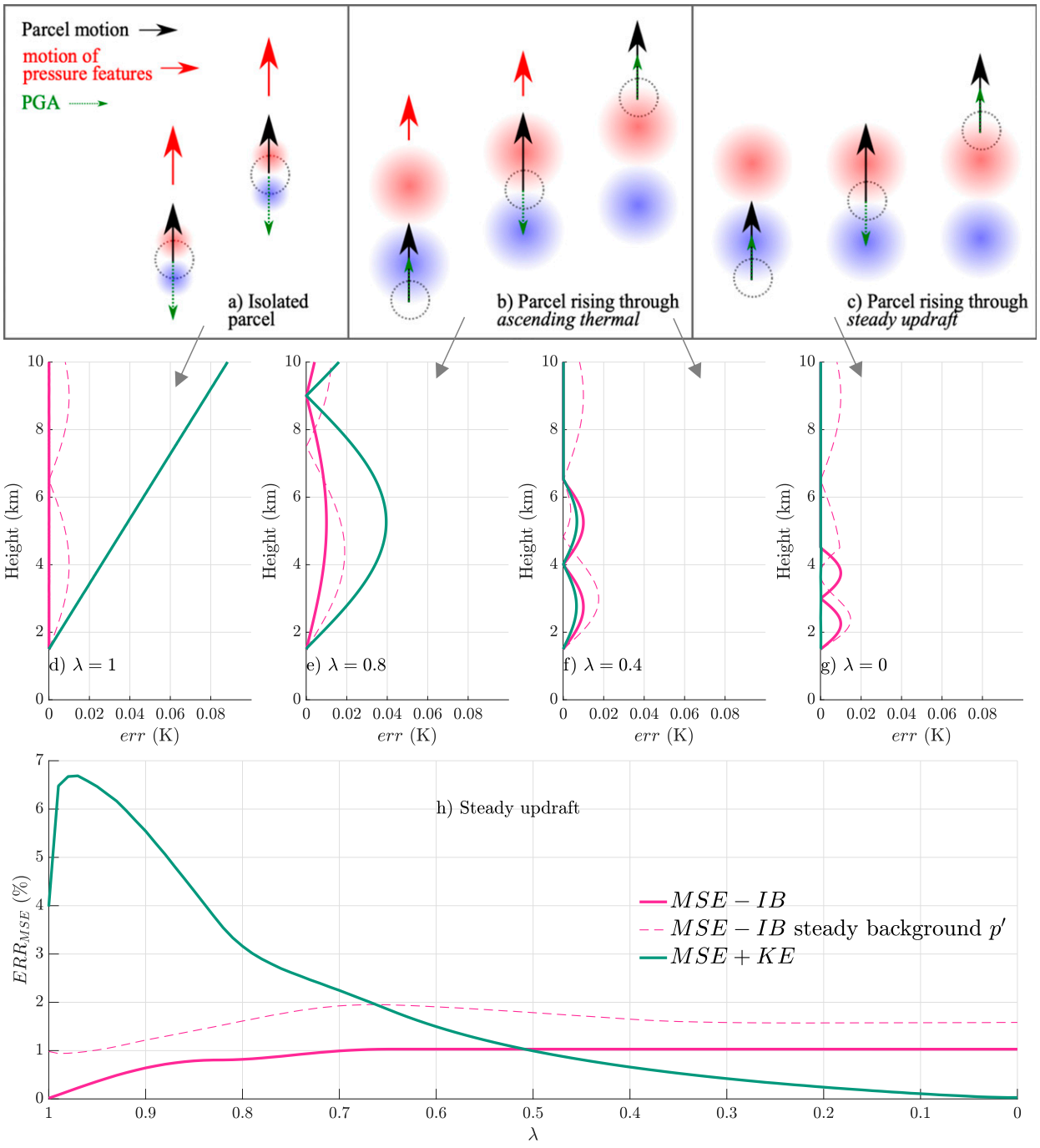

FIG. 1. (a)–(c) Schematics of the different scenarios for a parcel that interacts with a p' dipole, as a function of λ. Blue areas indicate negative p' and red areas indicate positive p'. (a) A parcel rises at the same rate as the p' dipole (i.e., $\lambda \to 1$). (b) Both the parcel and dipole rise, but the parcel rises faster (akin to how parcels behave in moist thermals, i.e., $0 < \lambda < 1$). (c) The dipole is steady as the parcel rises through it (i.e., $\lambda \to 0$). In the remaining panels, err (K) when MSE − IB conservation is assumed [e.g., Eq. (24); no background steady p': magenta solid line; steady background p': magenta dashed line] and MSE + KE conservation is assumed [e.g., Eq. (25); green solid line]. Vertical profiles are shown for (d) $\lambda = 1$: (e) $\lambda = 0.8$, (f) $\lambda = 0.4$, and (g) $\lambda = 0$. (h) $\mathrm{ERR}_{\mathrm{MSE}'}$ (y axis) as a function of λ (x axis), where we have normalized by an MSE′ of c_p (J kg^{-1}). The seemingly spurious decrease in the green line at $\lambda = 1$ is simply an artifact of the sinusoidal shape of the p' distribution and the fact that we have assessed errors over a restricted region below 10 km.

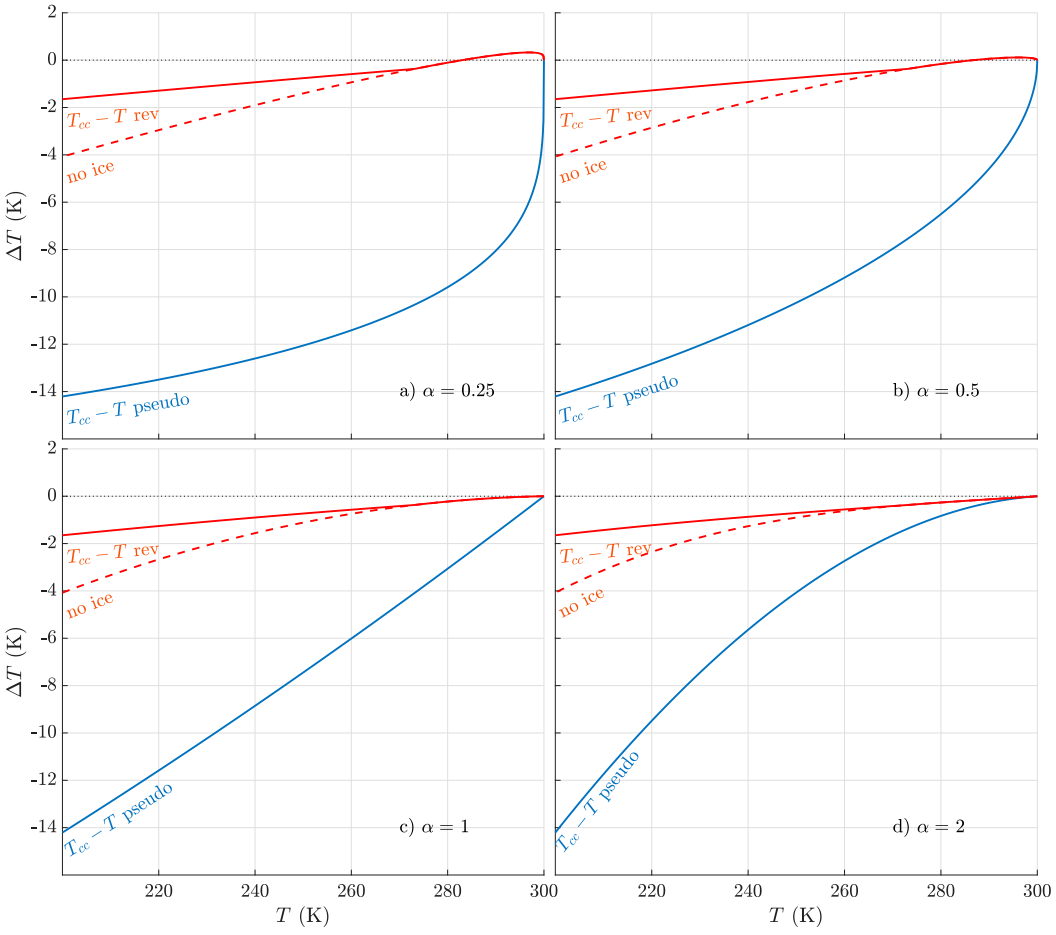

FIG. 2. Solutions to Eq. (30) (K) for pseudo ascent (blue lines), rev ascent with liquid only (red dashed lines), and rev ascent with liquid and ice (red solid lines). Values of the parameter α, which determine the shape of the profile of q_v, are (a) 0.25, (b) 0.5, (c) 1, and (d) 2.

nonnegligible factor that is as large as 5% when substantial condensate is present. When we neglect the influence of water on heat capacity, we underestimate the heat capacity of the air parcel. Thus, as a parcel expends energy doing work as it rises, it will cool more strongly when a constant heat capacity is used than when the moisture dependency of heat capacities are considered. This concept is demonstrated quantitatively through a simple comparison of the eqs. for MSE and $\mathrm{MSE_{cc}}$. Consider two rising parcels: one conserves its $\mathrm{MSE_{cc}}$, and another conserves its MSE. For simplicity, we assume both parcels maintain identical q_v. Because of these assumptions, the parcels must have different temperatures as they rise, denoted as T for the parcel that conserves MSE and T_{cc} for the parcel that conserves $\mathrm{MSE_{cc}}$. Taking $\mathrm{MSE_{cc}} - \mathrm{MSE}$ for this situation gives

$$\mathrm{MSE_{cc}} - \mathrm{MSE} = c_{pd}(T_{\mathrm{cc}} - T) + q_v[(c_{pd} - c_{pv})T + T_{\mathrm{ref}}(c_{pv} - c_l)] - q_i T_{\mathrm{ref}}(c_l - c_i) + q_l T(c_{pd} - c_l) + q_i T(c_{pd} - c_i). \quad (28)$$

If the parcels begin their ascent at an identical temperature T_b and water vapor mass fraction $q_{v,b}$, we may also write the following:

$$\mathrm{MSE_{cc}} - \mathrm{MSE} = q_{v,b}[(c_{pd} - c_{pv})T_b + T_{\mathrm{ref}}(c_{pv} - c_l)]. \quad (29)$$

Combining Eqs. (28) and (29) and solving for $T_{\mathrm{cc}} - T$ yields the following:

$$T_{\mathrm{cc}} - T = c_{pd}^{-1}[(c_{pd} - c_{pv})(q_{v,b}T_b - q_v T + (q_{v,b} - q_v)(c_{pv} - c_l)T_{\mathrm{ref}}) + q_i T_{\mathrm{ref}}(c_l - c_i) + q_l T(c_l - c_{pd}) + q_i T(c_i - c_{pd})]. \quad (30)$$

For a pseudoadiabatic (hereafter "pseudo") parcel $q_l = q_i = 0$ on the right hand side (RHS) of Eq. (30) will be negative for typical parameter values, and hence $T_{\mathrm{cc}} < T$. The parcel will therefore remain cooler during ascent when we neglect moisture influences on heat capacity and assume constant latent heats, compared to when we account for these effects. This result is confirmed by evaluating Eq. (30) with a simple linear profile of T ranging from 300 to 200 K and a profile of $q_v(T) = 0.016[(T - 200)/100]^{\alpha}$, wherein q_v gradually decreases from 0.016 kg kg^{-1} at $T = 300$ K to 0 kg kg^{-1} at $T = 200$ K. For these profiles, $T_{\mathrm{cc}} - T$ becomes increasingly negative as T and q_v decrease (Fig. 2 shows results for $\alpha = 0.25, 0.5, 1, 2$).

For a parcel undergoing reversible adiabatic ascent (hereafter "rev"), $q_l T(c_l - c_{pd}) > 0$ and $q_i T(c_i - c_{pd}) > 0$, which makes it difficult to outright determine whether the RHS of Eq. (30) should be positive or negative by simply looking at the equation. However, in using the simple T and q_v profiles from the previous paragraph, we find that the RHS of Eq. (30) is indeed typically negative for both liquid only and liquid + ice processes (Fig. 2). This means that we will also underestimate lifted parcel T for rev ascent when we neglect moisture influences on heat capacity and assume constant latent heats, though to a lesser extent than for pseudo ascent. Thus, generally, we expect MSE formulae with constant coefficients to underestimate the T for lifted air parcels that achieve $B > 0$.

3. Numerical simulations

Trajectories are analyzed in four different simulations to evaluate the conserved variables discussed in the previous section. These simulations are summarized as:

- Disorganized nonsupercellular deep convection (hereafter WK DS) in an environment with weak vertical wind shear.
- A supercell thunderstorm (hereafter SUP) in an environment with strong vertical wind shear.
- A midlatitude squall line occurring with weak vertical wind shear (hereafter WS SL).
- A midlatitude squall line occurring with strong vertical wind shear (hereafter SS SL).

The WK DS is our closest analog to past studies of disorganized deep convection (e.g., Sherwood et al. 2013; Romps and Charn 2015; Hernandez-Deckers and Sherwood 2016), where p' generally has small magnitude and its structures are highly transient; hence MSE − IB is expected to be well-conserved. However, in nature convection is often organized into coherent structures. The other three experiments therefore represent comparatively organized forms of convection that may be expected to yield different behavior in p' than in the WK DS case. Weakly sheared squall lines (WS SL) (e.g., Lebo and Morrison 2015) often also produce relatively transient p' structures which are primarily tied to rising cloud thermals. Strongly sheared squall lines (SS SL) and supercell thunderstorms (SUP) often feature persistent quasi-steady updraft structure (e.g., Rotunno et al. 1988; Peters et al. 2019, 2020d,c) distributions of p' (e.g., Bryan and Rotunno 2014; Rotunno and Klemp 1982). Thus, our experiment is designed to assess the influence of p' magnitude and steadiness on errors related to the conservation assumptions derived in the previous section, and to do so for both disorganized and organized forms of convection.

All simulations use Cloud Model 1 (CM1; e.g., Bryan and Fritsch 2002) version 19 with a compressible equation and an acoustic time-splitting integration scheme. All thermodynamic constants in subsequent calculations are set to their values found in the constants.F module of CM1, available at https://www2.mmm.ucar.edu/people/bryan/cm1/getcode.html. CM1 uses a prognostic equation for θ, and all thermodynamic equations use moisture dependent heat capacity and temperature dependent latent heat formulae that are identical to what was used in the section 2 derivations. The double moment microphysics scheme of Morrison et al. (2009) was used to parameterize microphysical processes, with the prognostic rimed ice species set to hail. All radiation and surface fluxes were turned off, and the "free-slip" option was used for top and bottom boundary conditions. All simulations included initial random T perturbations with a maximum amplitude of 0.25 K to facilitate the development of turbulence. Finally, all simulations were initialized with a passive tracer within the lowest 1.5 km of the model domain to quantify parcel dilution. A total of 1000 unique forward-moving parcel trajectories were released in each simulation and allowed to ascend through deep convective updrafts. These parcel trajectories were run in-line with model integration using the "built-in" software within CM1, and model variables were output from these trajectories at each model time step. These trajectory time series were used to evaluate budgets from the previous section.

The SUP simulation was originally used in Peters et al. (2021, 2020c). This simulation featured domain dimensions of 108 km in the x and y directions, and 22 km in the vertical direction, with a 100-m isotropic grid spacing. Lateral boundary conditions were "open radiative" (e.g., Durran and Klemp 1983). Convection was initiated by including a 1-K Gaussian shaped warm bubble with a horizontal radius of influence of 10 km, a vertical radius of influence of 1 km, a horizontal center in the domain center, and a vertical center at 500 m. The initial thermodynamic profile was generated using the analytic formulae of Weisman and Klemp (1982) (hereafter WK82), which was modified with constant relative humidity of 45% above 3 km. The wind profile featured unidirectional vertical wind shear, with no variation in v wind with height, a constant linear increase in u wind of 42.5 m s^{-1} between heights of 0 and 6 km, and u wind held constant above 6 km at its 6 km value. The simulation was run for 4 h. Forward trajectories were released at hour 2 within the distant inflow region to the supercell (approximately 45 km away), at initial heights between 0 and 1 km. The trajectories that ascended through the updraft entered between 3 and 3.5 h from the southeast. Additional details of this modeling configuration are available in Peters et al. (2020c). In the WK DS simulation, the u increase with height was set to 7.5 m s^{-1}, with all other attributes identical to that of the SUP simulation.

The squall-line simulations originate from Mulholland et al. (2021). These simulations share many of the same configurations as the SUP and WK DS runs (e.g., diffusion, subgrid-scale parameterization, microphysics parameterization, top and bottom boundary conditions), but with the following important differences. The domain dimensions were 420 km in the x direction, 99 km in the y direction, and 25 km in the z direction. The horizontal and vertical grid spacing was 250 m. Lateral boundary conditions were open radiative in the x direction, and periodic in the y direction. A squall line was initiated by including a 2.5 km deep cold pool in the initial conditions with a negative T perturbation of −5 K at the surface, and a linear decrease in the magnitude of the T perturbation to 0 K at 2.5 km. The initial thermodynamic profile once again followed the WK82 analytic formulae, with a boundary layer q_v of 14 g kg^{-1} and a surface temperature of 302 K. In the WS SL

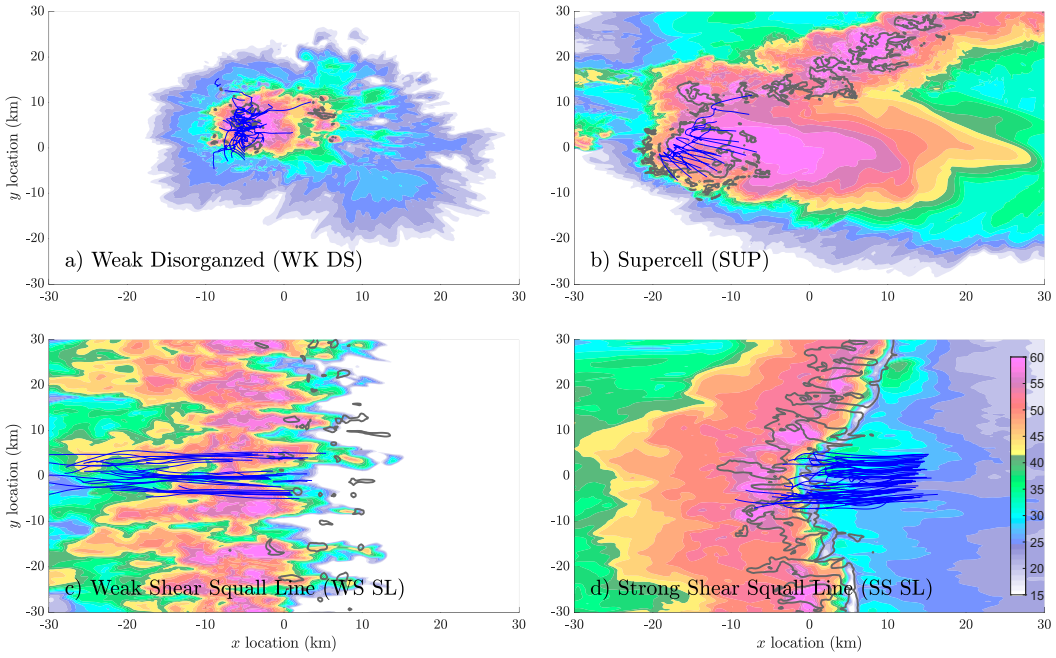

FIG. 3. Plan views of simulated radar reflectivity factor at 1 km (shading, dBZ), maximum column $w = 20\,\mathrm{m\,s^{-1}}$ (gray contours), and selected trajectory paths (blue lines), showing only the portion of the path where $w > 0.5\,\mathrm{m\,s^{-1}}$. (a) The WK DS simulation at 1 h, (b) the SUP simulation at 3 h 10 min, (c) the WS SL simulation at 7 h, and (d) the SS SL simulation at 7 h.

simulation, the surface wind outside the cold pool was set to $-7\,\mathrm{m\,s^{-1}}$, increased linearly to $0\,\mathrm{m\,s^{-1}}$ at 2.5 km, and was set to $0\,\mathrm{m\,s^{-1}}$ elsewhere outside the cold pool, and everywhere inside the cold pool. In the SS SL simulation, the surface wind outside the cold pool was set to $-26\,\mathrm{m\,s^{-1}}$, increased linearly to $0\,\mathrm{m\,s^{-1}}$ at 2.5 km, increased linearly to $10\,\mathrm{m\,s^{-1}}$ at 10 km, was held constant at $10\,\mathrm{m\,s^{-1}}$ above 10 km, and set to $0\,\mathrm{m\,s^{-1}}$ everywhere inside the cold pool. Both the WS SL and SS SL simulations were run for 8 h, with trajectories initialized at 4 h on the convectively unmodified side of the simulation, and the approximate time that trajectories passed through deep convective updrafts occurring at 5 h.

A multicellular cluster of deep convection evolved from the initial warm bubble in the WK DS simulation (Fig. 3a), achieving peak maximum domain w (not shown) at roughly 1 h into the integration. This peak in w approximately coincided with the time interval where trajectories entered and ascended through updrafts. A left- and right-moving supercell pair was produced by the initial warm bubble in the SUP simulation. The right mover achieved a quasi-steady updraft after 1.5 h of model integration that persisted through the end of the simulation (Fig. 3b). Trajectories entered and ascended through the right-moving supercell updraft approximately 3 h into the simulation (Fig. 3c). The WS SL featured scattered updrafts that moved substantially westward of the cold pool edge (Fig. 3c), whereas the SS SL featured comparatively interconnected updrafts that occurred in a larger concentration near the cold pool edge (Fig. 3d). Trajectories entered the squall lines and ascended through convection along the leading edge of the cold pool.

To concisely quantify errors, we examined normalized vertically integrated errors in predictions of $\mathrm{MSE}' = \mathrm{MSE} - \mathrm{MSE}_0$ and B. For example,

$$\mathrm{ERR_{MSE}} = \sqrt{\frac{\int_{z=z_i}^{z=z_f} (\mathrm{MSE}'_{\mathrm{pred}} - \mathrm{MSE}'_{\mathrm{traj}})^2\, dz}{\int_{z=z_i}^{z=z_f} \mathrm{MSE}'^2_{\mathrm{traj}}\, dz}}, \tag{31}$$

A value of $\mathrm{ERR}_{\psi'}$ of 0.05 indicates that errors in $\mathrm{MSE}'_{\mathrm{pred}}$ are roughly 5% as large as $\mathrm{MSE}'_{\mathrm{traj}}$. We would consider this to be a "small error" given its size relative to the overall magnitude of ψ'. In an alternative example, a $\mathrm{ERR_{MSE}}$ value of 0.9 indicates that errors in $\mathrm{MSE}'_{\mathrm{pred}}$ are nearly as large (90%) as the magnitude of $\mathrm{MSE}'_{\mathrm{traj}}$. We would therefore consider this later example to be a "large error." In a similar manner, the biases are defined as follows:

$$\mathrm{BIAS_{MSE}} = \frac{\frac{1}{z_f - z_i}\int_{z=z_i}^{z=z_f} (\mathrm{MSE}'_{\mathrm{pred}} - \mathrm{MSE}'_{\mathrm{traj}})\, dz}{\sqrt{\frac{1}{z_f - z_i}\int_{z=z_i}^{z=z_f} \mathrm{MSE}'^2_{\mathrm{traj}}\, dz}}. \tag{32}$$

Similar expressions were used to obtain ERR_B and BIAS_B. To isolate the parts of trajectories that ascend through updrafts in all subsequent trajectory calculations, the top z_f and bottom z_i bounds of this integration bound a region where w continuously exceeded $0.5\,\mathrm{m\,s^{-1}}$, and wherein w achieved its maximum value. All quantitative differences discussed below are

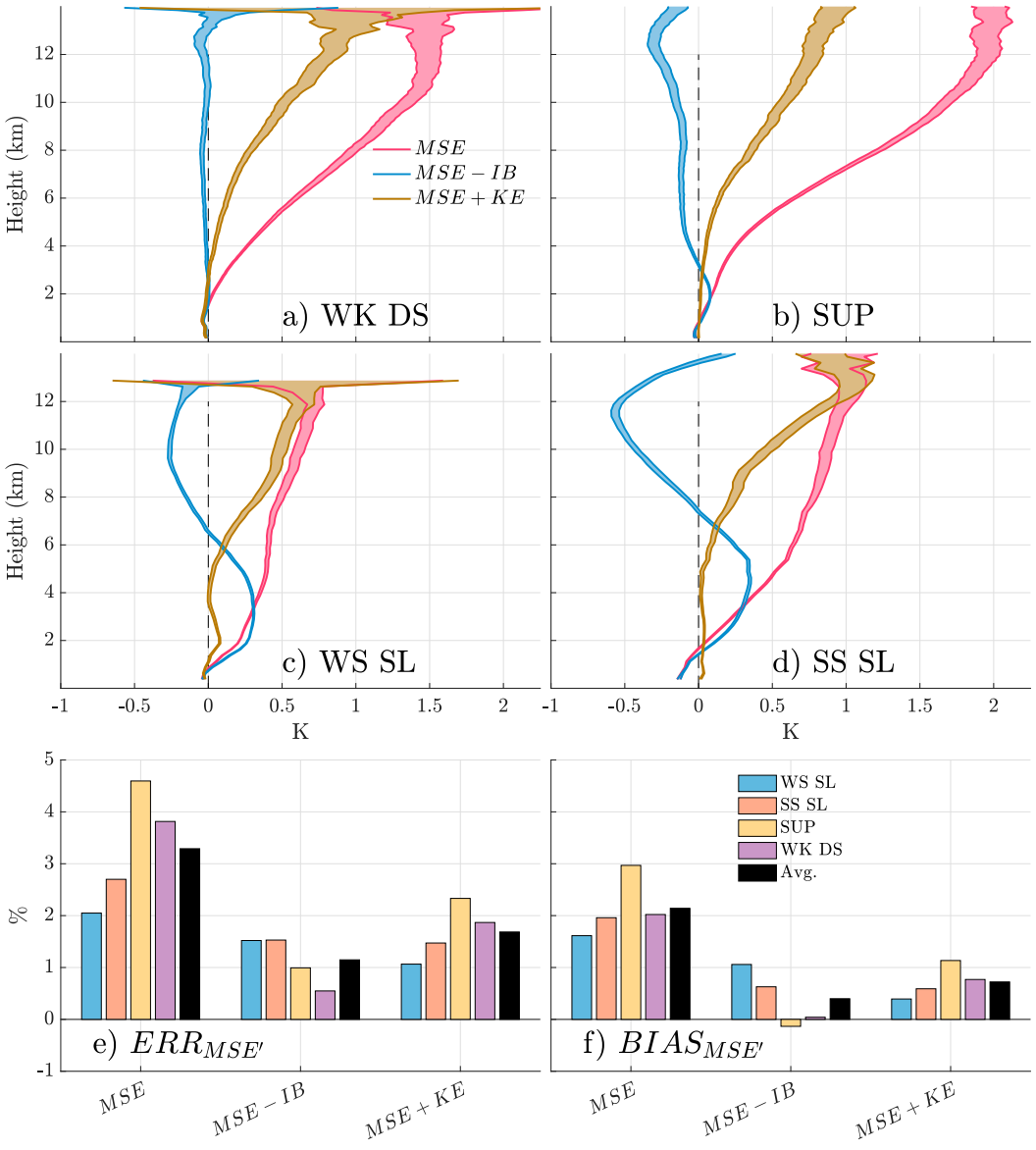

FIG. 4. Vertical profiles of the average errors in MSE/c_{pd} (K, x axis) prediction as a function of height (km, y axis) along trajectories associated with each of the individual conservation laws. Colors correspond to the conservation laws indicated in the legend in (a). The width of the shaded region represents the 5th–95th percentile confidence bounds for the average at that height, as determined by the Student's t test. (a) The WK DS simulation, (b) the SUP simulation, (c) the WS SL simulation, and (d) the SS SL simulation. (e) Percentage errors and (f) biases in the prediction of the vertical profile of MSE′ for the different conservation laws [see the legend in (f) for the color correspondence with individual simulations]. Black bars show the (e) average errors and (f) biases.

statistically significant to the 95% confidence level based on the Student's t test.

4. Results

a. *Predictions of updraft MSE′ profiles*

We begin by comparing how accurately the conservation equations for MSE, MSE + KE, and MSE − IB describe the evolution of MSE along trajectory paths. All numerical integrations in this subsection were computed using the trapezoid rule. Unsurprisingly, $\mathrm{ERR_{MSE}}$ was the largest in all simulations (Figs. 4a–d). In WK DS, $\mathrm{ERR_{MSE-IB}}$ was small throughout the depth of the troposphere (Fig. 4a), indicating that MSE − IB was indeed very close to adiabatically conserved in this simulation. Slightly larger errors related to MSE − IB were present in the SUP simulation (Fig. 4b), but this variable was still better conserved than MSE + KE though most of the troposphere. In the squall-line simulations, maximum $\mathrm{ERR_{MSE-IB}}$ and $\mathrm{ERR_{MSE+KE}}$ were generally comparable (Figs. 4c,d), with $\mathrm{ERR_{MSE+KE}}$ smallest below 6 km and $\mathrm{ERR_{MSE-IB}}$ smallest

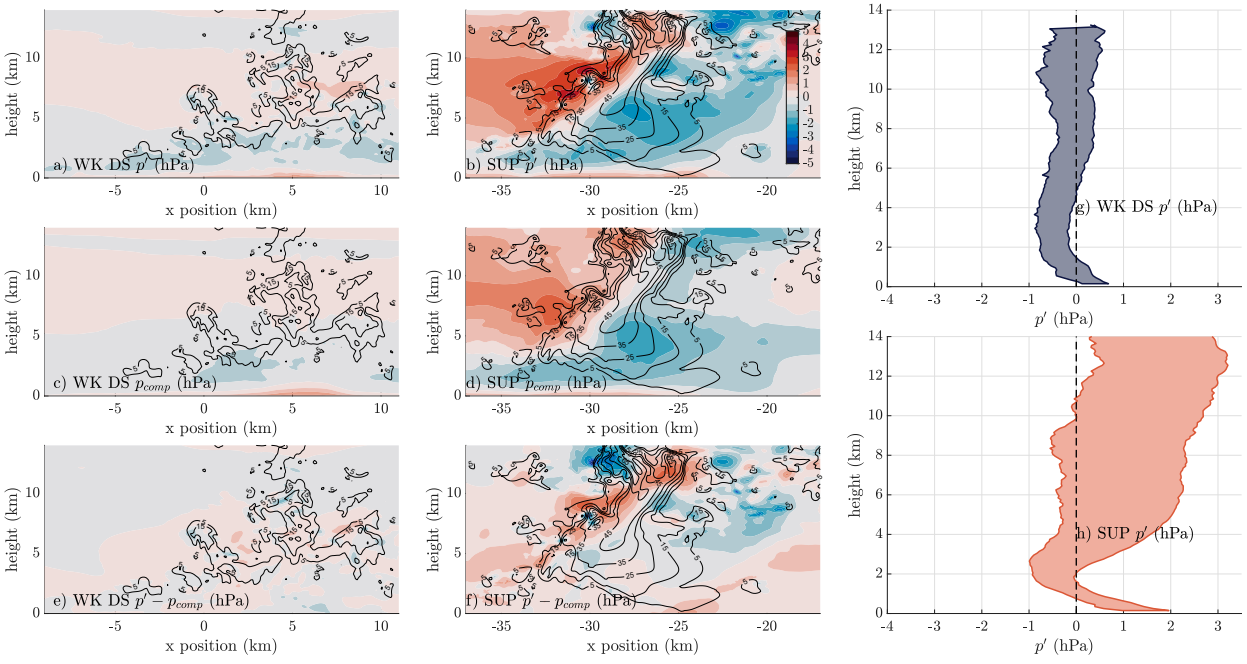

FIG. 5. (a),(b) Instantaneous snapshots oriented in the x (x axis) and z (y axis) directions of p' (hPa, shading) and w (contours, intervals of 10 m s^{-1} starting at 5 m s^{-1}), valid at (a) output time 1 h 15 min in the WK DS simulation, and (b) output time 3 h 15 min in the SUP simulation. (c),(d) As in (a) and (b), but showing p'_{comp} (shaded, hPa). (e),(f) As in (a) and (b), but showing $p' - p'_{\text{comp}}$ (shaded, hPa), valid at the same time as (a) and (b). (g),(h) The 10th–90th-percentile range of p' along trajectories in (g) the WK DS simulation and (h) the SUP simulation.

above 6 km. Across all simulations, MSE + KE steadily accumulated positive error with height, in a similar manner to our toy model example in Fig. 1d. In contrast, MSE − IB incurred positive errors at low levels that reversed sign and became negative at upper levels. Percentage errors (Fig. 4e) and biases (Fig. 4f) in MSE′ prediction were minimized overall for MSE − IB, though MSE + KE performed slightly better in the squall-line simulations.

What is the take home message? Assuming that MSE − IB is adiabatically conserved is a superior assumption in the SUP and WK DS simulations—both isolated convective modes. Whereas assuming MSE − IB or MSE + KE are adiabatically conserved give similar error magnitudes in the squall-line simulations with a slight edge toward MSE + KE. Both variables are superior to assuming MSE alone is adiabatically conserved. The overall magnitude of these percentage errors may seem small, but as will be shown later, small errors in MSE′ may translate to comparatively large errors in the predictions of quantities such as B.

b. *Reason for error differences between MSE − IB and MSE + KE*

What is responsible for these differences in errors related to MSE + KE and MSE − IB among the simulations? Recall that errors for both MSE − IB and MSE + KE relate to neglected p' effects. The former quantity neglects parcel pressure-volume work done by p' all together, whereas the latter quantity assumes that p' is steady. Thus, we analyze the behavior of p' among simulations and relate this behavior to our toy model in section 2d, to understand how both of these assumptions regarding p' lead to errors. We examine both instantaneous p' and 15 min composites p'_{comp} of 5 s model output to represent quasi-steady p' features; the quantity $p' - p'_{\text{comp}}$ then represents instantaneous nonsteady deviations from the quasi-steady p' features.

In the WK DS simulation, there was no obvious spatial reference point from which to compute p_{comp} owing to its disorganized nature, and we therefore computed a temporal average of the domain. In the WS SL and SS SL simulations, p_{comp} was computed as the two-dimensional along-line and time average of p', centered at the right-most location of $T' < 1$ K at the surface at each y location. Finally, in the SUP simulation, p_{comp} was defined as the temporal average within a domain subset that was horizontally centered at the location of the domain maximum w at each time.

WK DS $|p'|$ was generally small compared to those of the other simulations (Figs. 5a,c,e). There was a broad region of negative p_{comp} in the lower troposphere (Fig. 5c), and comparatively small p_{comp} in the middle-to-upper troposphere (Fig. 5c). Transient p' features associated with rising thermals were present in the middle-to-upper troposphere (Fig. 5e), with $|p'|$ comparable to or larger than p_{comp} magnitude in the lower troposphere (Fig. 5c).

Comparatively large $|p'|$ was present in SUP simulation (Figs. 5b,d,f), with a large region of $p' < 0$ present in the "lower-right" quadrant of the updraft (Fig. 5b), and a large region of $p' > 0$ with comparable magnitude in the "upper-left" quadrant of the updraft (Fig. 5b). Such p' features are

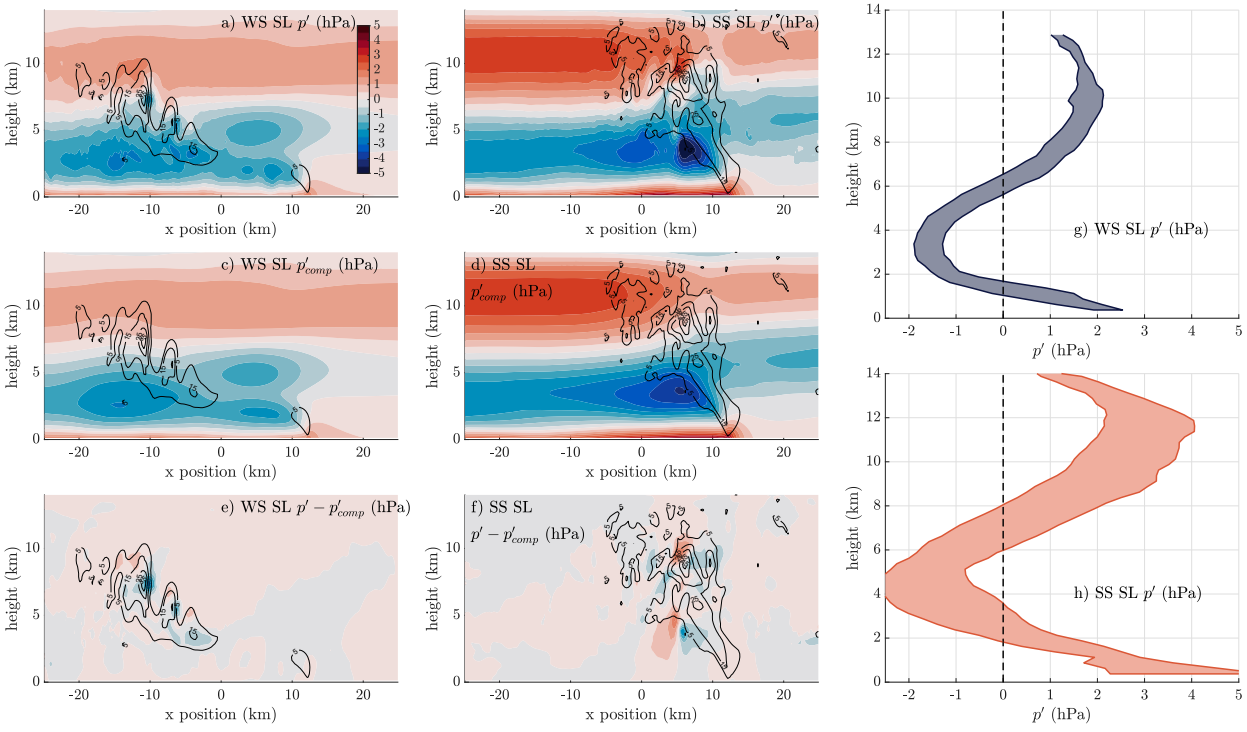

FIG. 6. As in Fig. 5, but for (a),(c),(e),(g) the WS SL simulation and (b),(d),(f),(h) the SS SL simulation.

common in supercells (e.g., Fig. 12 in Peters et al. 2019). In the lower troposphere, these p' features were predominantly steady, as indicated by large $|p'_{\text{comp}}|$ (Fig. 5d) and small $|p' - p'_{\text{comp}}|$ (Fig. 5f) below 5 km. Above 5 km, however, nonsteady $p' - p'_{\text{comp}}$ (Fig. 5f) became larger in magnitude than p'_{comp} (Fig. 5d). Thus, in the supercell there was a hybrid regime with both steady and nonsteady p' present, but with the nonsteady p' features having a slightly larger magnitude than the steady features.

Snapshots of p' from the WS SL (Fig. 6a) and SS SL (Fig. 6b) simulations reveal horizontally expansive negative p' at low-levels and equally horizontally expansive positive p' at upper levels, with both of these features having a much larger horizontal extent than the updrafts themselves. These broad features were predominantly associated with p'_{comp}, and were therefore quasi-steady (Figs. 6c,d). Such large and persistent p' regions of this magnitude are common in squall lines (e.g., see Fig. 18c in Bryan and Parker 2010), and occur because of large expanses of negative B near the surface in the cold pool, and large expanses of positive B aloft related to the anvil (e.g., see Fig. 19b in Bryan and Parker 2010). Superimposed upon this steady p' structure were scattered transient local $p' - p_{\text{comp}}$ regions in the immediate vicinity of the updrafts (Figs. 6e,f), with arguably slightly smaller magnitudes than that of p_{comp}. Thus p' in the squall-lines, like in the case of the SUP simulation, were characterized by a hybrid regime of both steady and nonsteady p'. However, the steady p'_{comp} in the squall lines was more expansive and larger in magnitude than $p_{\text{comp}} - p'$, whereas in the case of the supercells the horizontal expanse of p'_{comp} and $p_{\text{comp}} - p'$ were more comparable, and $p_{\text{comp}} - p'$ was larger in magnitude in the upper troposphere.

The general behavior of p' along trajectories mimicked that of p'_{comp} in all of the simulations (e.g., Figs. 5g,h). For instance, both the WK DS (Fig. 5g) and SUP (Fig. 5h) simulations featured negative p' at low levels in both the cross sections, and in their profiles of p' along trajectories (Figs. 5g,h). The SUP simulation also featured both positive p'_{comp} aloft (Fig. 5d) and positive p' along trajectories (Fig. 5h) aloft. The squall-line simulations both featured negative p'_{comp} at low levels and positive p'_{comp} aloft (Figs. 6c,d), with magnitudes that were larger than that of the WK DS and SUP simulations. The p' along trajectories in the squall-line simulations reflects this pattern (Figs. 6g,h). The magnitudes of transient p' were quite large in both the SUP (Fig. 5f) and squall-line simulations (Figs. 6e,f); however, comparably large-in-magnitude fluctuations away from the median were not present in p' along the trajectories, suggesting that parcels did not directly pass through these transient p' regions. Thus, steady p' played a dominant role in determining p' along trajectories. This hints that the most analogous situation in our simple toy model to all of our simulations is with $\lambda > 0.5$ and a steady background p' field present.

Indeed, there is evidence in past literature that $\lambda \approx 1$ is most appropriate for real deep convection. For instance, recall that parcels will tend to ascend faster than thermals themselves, which means that the situation in our simulations is analogous to the $\lambda > 0$ situations in the section 2d example (i.e., Figs. 1b,e,f). Direct measurements of λ from simulations are difficult, but past authors have investigated analogous quantities. For instance, the ratio $\alpha = [\max(w)]/W$, where $\max(w)$ is the maximum w within the center of a thermal and W is the

ascent rate of a thermal, is typically close to 0.55 (e.g., Romps and Charn 2015; Morrison and Peters 2018). Since parcels rising through thermals spend most of their time ascending slower than the max(w), but faster than W, we expect that $\alpha < \lambda \approx \overline{w}/W < 1$, where $\overline{w}$ is the average w of the parcel as it ascends through a thermal, and λ from our simple examples in section 2d is analogous to $\overline{w}/W$. Thus, the interactions between parcels and thermals is most analogous to the toy model with $\lambda \gg 0.55$. In these situations, our toy model demonstrates that errors associated with MSE + KE accumulate steadily with height, which is corroborated by the error curve for MSE + KE for all simulations in Fig. 4, which resemble the toy model with $\lambda = 1$ (Fig. 1d).

Finally, the magnitude errors related to MSE − IB among our simulations appear to be tied to the magnitude of the steady background p'. For instance, the largest MSE − IB errors occurred in the squall-line simulations, which also produced the largest magnitude of p_{comp}. The smallest MSE − IB errors occurred in the WK DS simulation, which also had the smallest magnitude of p_{comp}.

c. Predictions of updraft B

Accurately predicting updraft B is critical to realistically portraying updraft behavior in CPs and numerical models. Hence, we next evaluate the predictions for B along trajectories. Our B predictions use the following assumptions:

- To avoid potential additional errors related to predicting hydrometeors along parcel paths, we compare our predictions of B, which do not incorporate hydrometer loading, to the B output along trajectory paths with hydrometeor loading removed. However, hydrometer mass fractions output on trajectory paths were used to compute heat capacities in our predictions, and were used in the hydrometeor loading part of IB.
- All predictions use the background environmental pressure p_0 in line with its definition in Eq. (6). Note that this allows us to make the substitution $\theta'/\theta_0 = T'/T_0$ in Eq. (8).
- We assume a maximum q_v saturation of 100% with respect to liquid and/or ice, in accordance with the formulas in the appendix. This assumption is necessary to obtain profiles of updraft T and q_v from MSE, and is commonly used in idealized parcel calculations (e.g., Romps 2015), CPs (e.g., Romps 2016) and numerical models (e.g., Khairoutdinov and Randall 2003).
- Predictions of B that assume MSE + KE is conserved use KE_{traj}.

All solutions for B were obtained by first solving for T using a Crank–Nicholson implicit integration scheme (as was described in Romps 2015), and by using the Clausius–Clapeyron equation to obtain a prediction q_v from T and the background pressure p_0.

We start by analyzing MSE, MSE + KE, and MSE − IB, which are the conserved variables derived using the least assumptions. All three predictions reasonably capture the shape of the simulated B profile (Figs. 7a–d). However, all three predictions also overestimate the magnitude of B—particularly above the freezing level (i.e., 6 km). Indeed, ERR_B were generally far larger (Fig. 7e, 15%–30%) than ERR_{MSE} (Fig. 4e, 0%–5%), suggesting that there are substantial sources of errors from the assumptions used to calculate B from MSE, such as the preclusion of supersaturation with respect to liquid and/or ice. Nonetheless, differences in B errors among the different conserved variables are instructive for quantifying the error contributions from neglected adiabatic processes. Conservation of MSE − IB yields the best prediction of B, and conservation of MSE yields the worst prediction. Aggregate errors were on the order of 4%–15% smaller (Figs. 7e,g), and biases as much as 15% smaller (Figs. 7f,h), for MSE − IB than for MSE and MSE + KE.

It may seem contradictory that $ERR_{B,MSE-IB}$ and $BIAS_{B,MSE-IB}$ were the smallest in the squall-line runs, whereas $ERR_{MSE,MSE-IB}$ and $ERR_{MSE,MSE+KE}$ in these simulations were shown to be comparable. This apparent discrepancy is potentially a result of compensating errors associated with a general high bias in B predictions because of neglected supersaturation, which was compensated by an erroneous low BIAS in $ERR_{MSE,MSE-IB}$ aloft.

Both approximations that neglect moisture influences on heat capacity and assume latent heats (MSE_{cc} and $MSE_{cc,ni}$) underestimate B (Figs. 8a–d)—particularly in the case of the WS SL simulation (Fig. 8c). Unsurprisingly, this low bias is most pronounced when ice is neglected because of the absence of warming due to release of the latent heat of fusion; this bias is reduced when ice is included in the formulation. Aggregate errors (Fig. 8e) and biases (Fig. 8f) for these formulations are on the order of 2–3 times larger than those for MSE, MSE + KE, and MSE − IB (cf. with Figs. 7e,f).

A natural question is, what happens if we retain the $-wB$ term on the RHSs of the equations for MSE_{cc} and $MSE_{cc,ni}$? Recall that we had to assume that the parcel, in addition to the background environment, was hydrostatically balanced to make the $-wB$ term in Eq. (7) vanish, thereby obtaining the conservation law for MSE in Eq. (9). Surely retaining this term [as in Eq. (10) in Riehl and Malkus 1958], rather than dropping it, will result in more accurate predictions of B despite the moisture agnostic heat capacities and constant latent heats? What we find is the opposite. We call these new approximations MSE_{cc} − IB and $MSE_{cc,ni}$ − IB, respectively. MSE_{cc} − IB and $MSE_{cc,ni}$ − IB feature generally reduced estimates for B relative to the formulations without IB (Figs. 8a–d), making these estimates poorer matches for the actual B along trajectories. ERR (Figs. 8e,g) and BIAS (Figs. 8f,h) show 5%–10% increases over the formulations without the IB term.

Do the aforementioned differences in the accuracy of B predictions adversely affect predictions of the level of neutral buoyancy (LNB) height? To address this question, we define the LNB height as the last instance along each trajectory for which $B = 0\,m\,s^{-2}$. MSE, MSE + KE, and MSE − IB all share similarly small bias magnitudes (<0.3 km) in their predictions of the LNB height (Fig. 9), with bias minimized for MSE − IB. In contrast, LNB biases for the approximate expressions for MSE are all <−1 km (Fig. 9), and generally increased when IB was included in the formulation.

d. Reason for errors related to approximate latent heat and heat capacity formulae

Though conservation of MSE − IB yielded the most accurate parcel predictions than conservation of MSE, conservation of

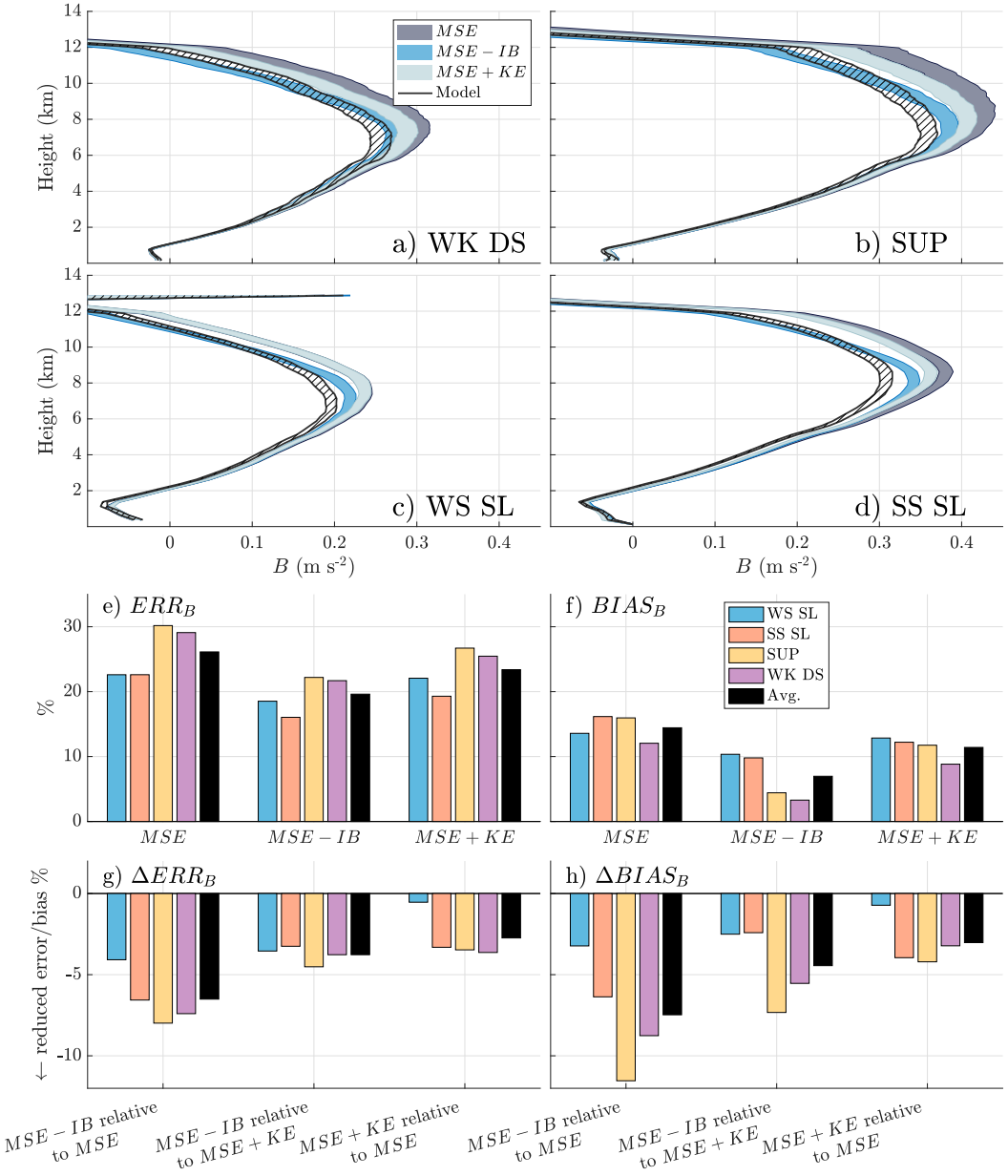

FIG. 7. (a)–(d) Predicted vertical profiles of B ($\mathrm{m\,s^{-2}}$, x axis) as a function of height (y axis) for the conserved variables indicted in the legend of (a), compared to B computed from trajectories in simulations (black hatched profiles). The range in a profile at a given height represents the 5th–95th-percentile confidence intervals on the value of the average over all trajectories at that height. (a) The WK DS simulation, (b) the SUP simulation, (c) the WS SL simulation, and (d) the SS SL simulation. (e),(f) As in Figs. 4e and 4f, but for predictions of B. (g) Error for MSE − IB minus the error for MSE (left, %), error for MSE − IB minus the error for MSE + KE (middle, %), and error for MSE + KE minus the error for MSE (right, %). (h) As in (g), but for bias.

$\mathrm{MSE_{cc}}$ − IB and $\mathrm{MSE_{cc,ni}}$ − IB yielded *less* accurate parcel predictions than $\mathrm{MSE_{cc}}$ and $\mathrm{MSE_{cc,ni}}$, respectively. This result may seem counterintuitive, but is explained by compensating errors. In the case of $\mathrm{MSE_{cc}}$ and $\mathrm{MSE_{cc,ni}}$, the sensible and latent energy of parcels is underestimated for reasons that will be described below. These approximations therefore yield underestimates of parcel B by itself. Because the IB term will only further reduce B in a positively buoyant updraft, adding this term only further underbiases B predictions.

Furthermore, the underestimations of B and the LNB height by $\mathrm{MSE_{cc}}$ are consistent with our theoretical analysis in section 2e. In particular, our analysis in that section showed that the underestimation of T and B by $\mathrm{MSE_{cc}}$ should be more

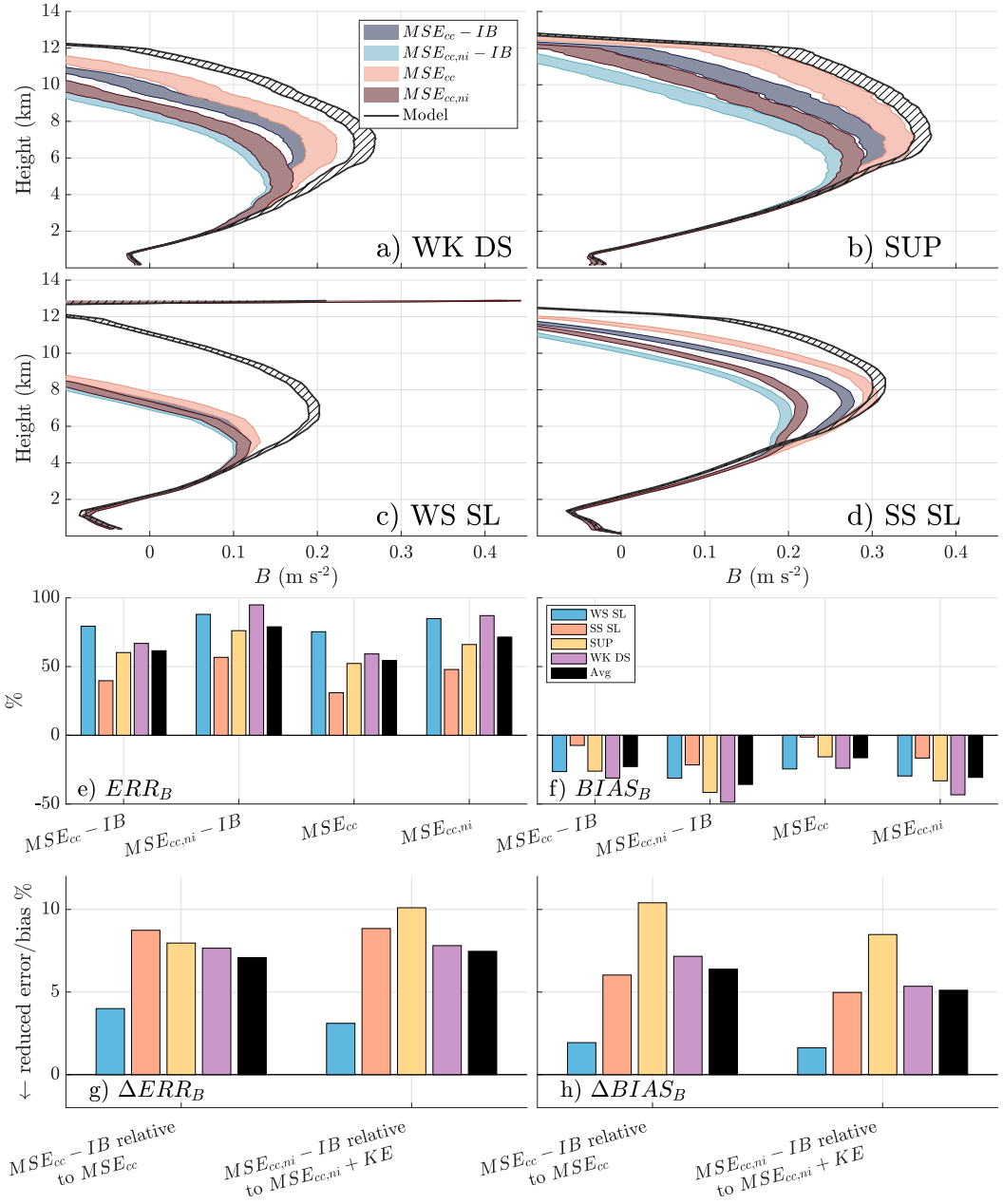

FIG. 8. As in Fig. 7, but for various approximate formulations for MSE.

pronounced for pseudo parcels, relative to rev parcels. This pseudo versus rev difference may partially explain why the MSE_{cc} and $MSE_{cc,ni}$ formulations produced more egregious errors in B prediction in some simulations (e.g., the WS SL simulation, Fig. 8c) than in others (e.g., the SUP simulation, Fig. 8b). Parcels in the WS SL simulation featured substantial q_t loss with height (Fig. 10a), exhibiting behavior closer to pseudo than rev ascent. Equation (30) tells us that the MSE formulations that neglect moisture influences on heat capacity and assume constant latent heats should severely underestimate parcel T in these situations, which is what happens aloft in the WS SL simulation. Parcels in the SUP simulation featured comparatively little q_t loss with height (Fig. 10b), exhibiting behavior closer to rev ascent. Equation (30) tells us that the MSE formulations that neglect moisture influences on heat capacity and assume constant latent heats should only modestly underestimate parcel T in these situations, which is what happens aloft in the SUP simulation. Thus, the accuracy of lifted parcel calculations based on the conservation of MSE with neglected moisture influences on heat capacity and constant latent heats may be strongly dependent on clouds' microphysical properties.

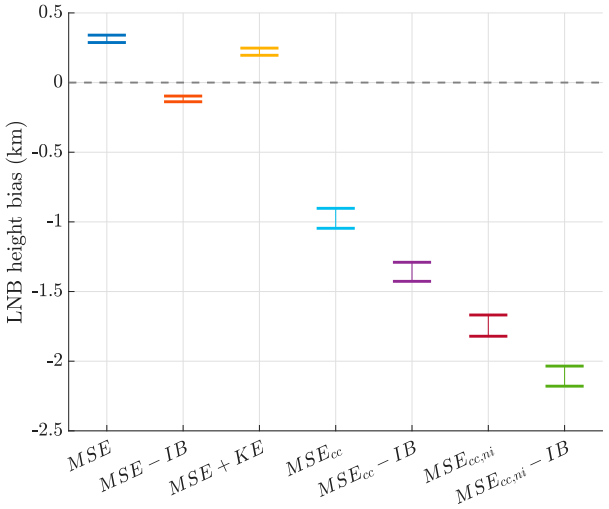

FIG. 9. The 5th–95th-percentile (based on the Student's t test) ranges of the mean bias in predicted LNB height (km, y axis) for different conserved variables (x axis).

5. Summary and conclusions

We have investigated the errors that occur when we assume the variables MSE, MSE − IB, MSE + KE, and various approximations for these quantities, are conserved in deep moist convection. These conserved variables are evaluated in their ability to predict the properties of parcel trajectories from simulations of deep moist convection. Our general conclusions are as follows:

- The most accurate predictions of simulated parcel B occur when it is assumed that MSE − IB is conserved, and when hydrometeor dependence of heat capacities and temperature dependencies of latent heats are included in this formula.
- Traditional approximations for MSE that neglect moisture influences on heat capacity and assume constant latent heats substantially underestimate parcel B and the LNB heights. This suggests that CAPE calculations, updraft calculations in CPs, and numerical models may all underestimate the B, depth, and intensity of deep convective updrafts.
- Amending traditional approximations for MSE with IB may actually make predictions of updraft B and LNB height less accurate because of compensating errors that occur with common approximate MSE formulations.
- A method for computing lifted parcel properties that assumes the adiabatic conservation of MSE − IB, includes variable heat capacities and latent heats, and includes mixed phase precipitation is advised for computing CAPE in convective environments with substantial ice and a mixed phase T range.

A particular limitation of this work is that we have only investigated deep moist convection with substantial ice content. Future work should investigate these ideas in the context of shallow convection. For instance, it is possible that the biases identified here are minimal in shallow convection and moderately deep cumulus congestus clouds that are dominated by warm microphysics. Future work should also quantify the differences in computation time for the different conservation methods, so that these computational differences can be weighed against the differences in accuracy.

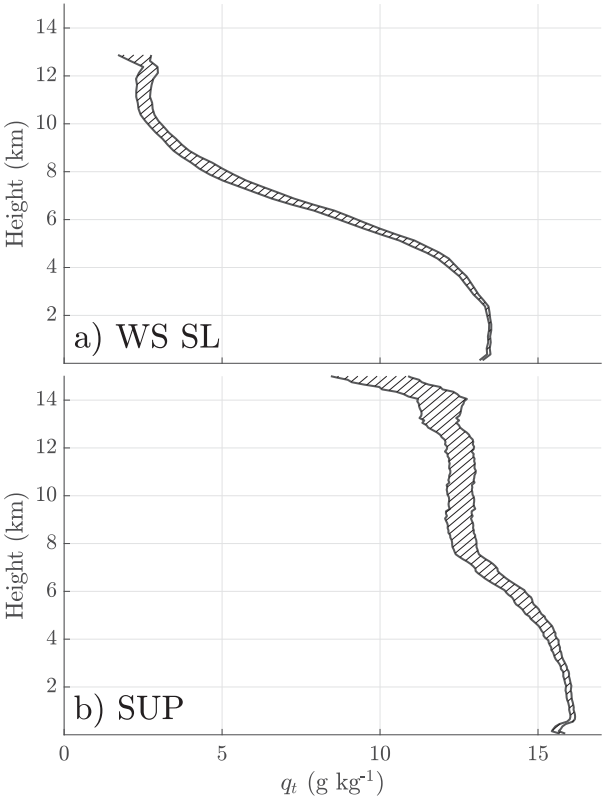

FIG. 10. As in Figs. 7b and 7c, but for vertical profiles of q_t (g kg^{-1}) from trajectories.

Acknowledgments. The authors thank Jake Mulholland, David Romps, Hugh Morrison, and an anonymous peer reviewer for helpful conversations and feedback. J. Peters's efforts were supported by National Science Foundation (NSF) Grants AGS-1928666 and AGS-1841674 and the Department of Energy Atmospheric System Research (DOE ASR) Grant DE-SC0000246356. D. Chavas was supported by NSF Grant AGS-1648681.

Data availability statement. Please reference Peters et al. (2020c) and Mulholland et al. (2021) for the model data used in this study.

APPENDIX

Saturation Mixing Ratios

The saturation vapor pressures over liquid $e_{s,l}$ and ice $e_{s,i}$ are determined in CM1 via the approximations from Bolton (1980):

$$e_{s,l} = 611.2e^{17.67(T-273.15)/(T-29.65)}, \quad \text{(A1)}$$

$$e_{s,i} = 611.2e^{21.874\,558\,4(T-273.15)/(T-7.66)}. \quad \text{(A2)}$$

The corresponding saturation mass fractions are the following:

$$q_{s,l} = \frac{R_d}{R_v}\frac{e_{s,l}}{p}, \quad \text{(A3)}$$

$$q_{s,i} = \frac{R_d}{R_v}\frac{e_{s,i}}{p}. \quad \text{(A4)}$$

For saturated calculations that neglect ice, $q_s = q_{s,l}$ is assumed to apply for all T. For calculations including ice, the partition function $\omega = \max\{\min[(T - 253.16)/20, 1], 0\}$ of Khairoutdinov and Randall (2003) is used, such that

$$q_s = \omega q_{s,l} + (1 - \omega)q_{s,i}. \quad \text{(A5)}$$

REFERENCES

Agard, V., and K. Emanuel, 2017: Clausius–Clapeyron scaling of peak CAPE in continental convective storm environments. *J. Atmos. Sci.*, **74**, 3043–3054, https://doi.org/10.1175/JAS-D-16-0352.1.

Arakawa, A., and W. H. Schubert, 1974: Interaction of a cumulus cloud ensemble with the large-scale environment, Part I. *J. Atmos. Sci.*, **31**, 674–701, https://doi.org/10.1175/1520-0469(1974)031<0674:IOACCE>2.0.CO;2.

Bolton, D., 1980: The computation of equivalent potential temperature. *Mon. Wea. Rev.*, **108**, 1046–1053, https://doi.org/10.1175/1520-0493(1980)108<1046:TCOEPT>2.0.CO;2.

Bryan, G. H., and J. M. Fritsch, 2002: A benchmark simulation for moist nonhydrostatic numerical models. *Mon. Wea. Rev.*, **130**, 2917–2928, https://doi.org/10.1175/1520-0493(2002)130<2917:ABSFMN>2.0.CO;2.

——, and ——, 2004: A reevaluation of ice–liquid water potential temperature. *Mon. Wea. Rev.*, **132**, 2421–2431, https://doi.org/10.1175/1520-0493(2004)132<2421:AROIWP>2.0.CO;2.

——, and M. D. Parker, 2010: Observations of a squall line and its near environment using high-frequency rawinsonde launches during VORTEX2. *Mon. Wea. Rev.*, **138**, 4076–4097, https://doi.org/10.1175/2010MWR3359.1.

——, and R. Rotunno, 2014: The optimal state for gravity currents in shear. *J. Atmos. Sci.*, **71**, 448–468, https://doi.org/10.1175/JAS-D-13-0156.1.

Darkow, G. L., 1968: The total energy environment of severe storms. *J. Appl. Meteor.*, **7**, 199–205, https://doi.org/10.1175/1520-0450(1968)007<0199:TTEEOS>2.0.CO;2.

Durran, D. R., and J. B. Klemp, 1983: A compressible model for the simulation of moist mountain waves. *Mon. Wea. Rev.*, **111**, 2341–2361, https://doi.org/10.1175/1520-0493(1983)111<2341:ACMFTS>2.0.CO;2.

Emanuel, K. A., 1994: *Atmospheric Convection*. Oxford University Press, 588 pp.

Hernandez-Deckers, D., and S. C. Sherwood, 2016: A numerical investigation of cumulus thermals. *J. Atmos. Sci.*, **73**, 4117–4136, https://doi.org/10.1175/JAS-D-15-0385.1.

Khairoutdinov, M., and D. A. Randall, 2003: Cloud resolving modeling of the ARM summer 1997 IOP: Model formulation, results, uncertainties, and sensitivities. *J. Atmos. Sci.*, **60**, 607–625, https://doi.org/10.1175/1520-0469(2003)060<0607:CRMOTA>2.0.CO;2.

Kiefer, P. J., 1941: The thermodynamic properties of water and water vapor. *Mon. Wea. Rev.*, **69**, 329–332, https://doi.org/10.1175/1520-0493(1941)069<0329:TTPOWA>2.0.CO;2.

Kreitzberg, C. W., 1964: The structure of occlusions as determined from serial ascents of vertically-directed radar. Air Force Cambridge Research Laboratory Rep. AFCRL-64-26, 121 pp.

Lebo, Z. J., and H. Morrison, 2015: Effects of horizontal and vertical grid spacing on mixing in simulated squall lines and implications for convective strength and structure. *Mon. Wea. Rev.*, **143**, 4355–4375, https://doi.org/10.1175/MWR-D-15-0154.1.

Morrison, H., and J. M. Peters, 2018: Theoretical expressions for the ascent rate of moist convective thermals. *J. Atmos. Sci.*, **75**, 1699–1719, https://doi.org/10.1175/JAS-D-17-0295.1.

——, G. Thompson, and V. Tatarskii, 2009: Impact of cloud microphysics on the development of trailing stratiform precipitation in a simulated squall line: Comparison of one and two-moment schemes. *Mon. Wea. Rev.*, **137**, 991–1007, https://doi.org/10.1175/2008MWR2556.1.

——, J. M. Peters, A. C. Varble, W. M. Hannah, and S. E. Giangrande, 2020: Thermal chains and entrainment in cumulus updrafts. Part I: Theoretical description. *J. Atmos. Sci.*, **77**, 3637–3660, https://doi.org/10.1175/JAS-D-19-0243.1.

Mulholland, J. P., J. M. Peters, and H. Morrison, 2021: How does vertical wind shear influence entrainment in squall lines? *J. Atmos. Sci.*, **78**, 1931–1946, https://doi.org/10.1175/JAS-D-20-0299.1.

Pauluis, O., 2008: Thermodynamic consistency of the anelastic approximation for a moist atmosphere. *J. Atmos. Sci.*, **65**, 2719–2729, https://doi.org/10.1175/2007JAS2475.1.

——, and I. M. Held, 2002: Entropy budget of an atmosphere in radiative-convective equilibrium. Part II: Latent heat transport and moist processes. *J. Atmos. Sci.*, **59**, 140–149, https://doi.org/10.1175/1520-0469(2002)059<0140:EBOAAI>2.0.CO;2.

Peters, J. M., C. Nowotarski, and H. Morrison, 2019: The role of vertical wind shear in modulating maximum supercell updraft velocities. *J. Atmos. Sci.*, **76**, 3169–3189, https://doi.org/10.1175/JAS-D-19-0096.1.

——, H. Morrison, A. C. Varble, W. M. Hannah, and S. E. Giangrande, 2020a: Thermal chains and entrainment in cumulus updrafts. Part II: Analysis of idealized simulations. *J. Atmos. Sci.*, **77**, 3661–3681, https://doi.org/10.1175/JAS-D-19-0244.1.

——, ——, C. J. Nowotarski, J. P. Mulholland, and R. L. Thompson, 2020b: A formula for the maximum vertical velocity in supercell updrafts. *J. Atmos. Sci.*, **77**, 3747–3757, https://doi.org/10.1175/JAS-D-20-0103.1.

——, C. J. Nowotarski, and G. L. Mullendore, 2020c: Are supercells resistant to entrainment because of their rotation? *J. Atmos. Sci.*, **77**, 1475–1495, https://doi.org/10.1175/JAS-D-19-0316.1.

——, ——, J. P. Mulholland, and R. L. Thompson, 2020d: The influences of effective inflow layer streamwise vorticity and storm-relative flow on supercell updraft properties. *J. Atmos. Sci.*, **77**, 3033–3057, https://doi.org/10.1175/JAS-D-19-0355.1.

——, H. Morrison, G. J. Zhang, and S. W. Powell, 2021: Improving the physical basis for updraft dynamics in deep convection parameterizations. *J. Adv. Model. Earth Syst.*, **13**, e2020MS002282, https://doi.org/10.1029/2020MS002282.

Riehl, H., and J. S. Malkus, 1958: On the heat balance in the equatorial trough zone. *Geophysica*, **6**, 503–538.

Romps, D. M., 2015: MSE minus CAPE is the true conserved variable for an adiabatically lifted parcel. *J. Atmos. Sci.*, **72**, 3639–3646, https://doi.org/10.1175/JAS-D-15-0054.1.

——, 2016: The stocastic parcel model: A deterministic parameterization of stochastically entraining convection. *J. Adv. Model. Earth Syst.*, **8**, 319–344, https://doi.org/10.1002/2015MS000537.

——, and Z. Kuang, 2010: Do undiluted convective plumes exist in the upper troposphere? *J. Atmos. Sci.*, **67**, 468–484, https://doi.org/10.1175/2009JAS3184.1.

——, and A. B. Charn, 2015: Sticky thermals: Evidence for a dominant balance between buoyancy and drag in cloud updrafts. *J. Atmos. Sci.*, **72**, 2890–2901, https://doi.org/10.1175/JAS-D-15-0042.1.

Rotunno, R., and J. B. Klemp, 1982: The influence of the shear-induced pressure gradient on thunderstorm motion. *Mon. Wea. Rev.*, **110**, 136–151, https://doi.org/10.1175/1520-0493(1982)110<0136:TIOTSI>2.0.CO;2.

——, ——, and M. L. Weisman, 1988: A theory for strong, long-lived squall lines. *J. Atmos. Sci.*, **45**, 463–485, https://doi.org/10.1175/1520-0469(1988)045<0463:ATFSLL>2.0.CO;2.

Sherwood, S. C., D. Hernandez-Deckers, and M. Colin, 2013: Slippery thermals and the cumulus entrainment paradox. *J. Atmos. Sci.*, **70**, 2426–2442, https://doi.org/10.1175/JAS-D-12-0220.1.

Sun, W.-Y., and O. M. Sun, 2015: Bernoulli equation and flow over a mountain. *Geosci. Lett.*, **2**, 7, https://doi.org/10.1186/s40562-015-0024-1.

——, and ——, 2019: Revisiting the parcel method and CAPE. *Dyn. Atmos. Oceans*, **86**, 134–152, https://doi.org/10.1016/j.dynatmoce.2019.03.008.

Weisman, M. L., and J. B. Klemp, 1982: The dependence of numerically simulated convective storms on vertical wind shear and buoyancy. *Mon. Wea. Rev.*, **110**, 504–520, https://doi.org/10.1175/1520-0493(1982)110<0504:TDONSC>2.0.CO;2.

Zhang, G. J., 2009: Effects of entrainment on convective available potential energy and closure assumptions in convective parameterization. *J. Geophys. Res.*, **114**, D07109, https://doi.org/10.1029/2008JD010976.

——, and N. A. McFarlane, 1991: Convective stabilization in midlatitudes. *Mon. Wea. Rev.*, **119**, 1915–1928, https://doi.org/10.1175/1520-0493(1991)119<1915:CSIM>2.0.CO;2.

——, and ——, 1995: Sensitivity of climate simulations to the parameterization of cumulus convection in the Canadian climate center general-circulation model. *Atmos.–Ocean*, **33**, 407–446, https://doi.org/10.1080/07055900.1995.9649539.